Multi-Objective Optimization Design of Fractional Slot Concentrated Winding Permanent Magnet Synchronous Machines

SALEH O. EDHAH[ID], **(Student Member, IEEE), JAMAL Y. ALSAWALHI**[ID], **(Member, IEEE), AND AHMED A. AL-DURRA**[ID] **(Senior Member, IEEE)**

Advanced Power and Energy Center, Electrical Engineering and Computer Science, Khalifa University of Science and Technology, Abu Dhabi, United Arab Emirates

Corresponding author: Saleh O. Edhah (saoedhah@pi.ac.ae)

ABSTRACT Fractional-slot concentrated-winding (FSCW) permanent magnet synchronous machines (PMSMs) have several advantages when compared to other conventional topologies. Design of these motors often rely on the designer's experience, or numerical methods which are time inefficient. This makes them unsuitable for multi-objective optimization design procedure in which a huge design space is adopted, and which have been shown to be effective in finding optimum machine designs. This work introduces a generic multi-objective optimization design framework for a surface mounted (SM) FSCW-PMSM based on a general analytical model that considers various machine aspects such as its geometry, winding configuration, losses, iron temporal flux density levels and drive control. The design procedure is demonstrated to design a surface-mounted (SM) FSCW-PMSM motor with a wide constant power speed range of 5:1. Validation is carried out using Finite Element Analysis (FEA) with good agreement in results.

INDEX TERMS Fractional-slot, permanent magnet synchronous machines, concentrated winding, multi-objective optimization design, motor optimization design, FSCW-PMSM.

I. INTRODUCTION

Various emerging applications such as electric vehicles (EV) and robotics demand high performance motors and generators with high power and torque densities, high efficiency at multiple operating points, high reliability and easy control. Out of the many different classes of electric machines, Permanent Magnet Synchronous Machines (PMSMs) have demonstrated excellent performance in these metrics.

The performance of PMSMs is directly affected by a ratio n_{spp} defined as the number of stator slots per rotor poles per phase. Based on its value, the machine can be classified into three main categories: Fractional-Slot Concentrated-Winding (FSCW) machine, Fractional-Slot Distributed-Winding (FSDW) machine, or Integer-Slot Distributed-Winding (ISDW) machine [1]. A FSCW-PMSM has $n_{spp} < 1$ and is equipped with winding coils that span one stator tooth pitch; a sample FSCW-PMSM is shown in Fig. 1.

The associate editor coordinating the review of this manuscript and approving it for publication was Xiaodong Sun[ID].
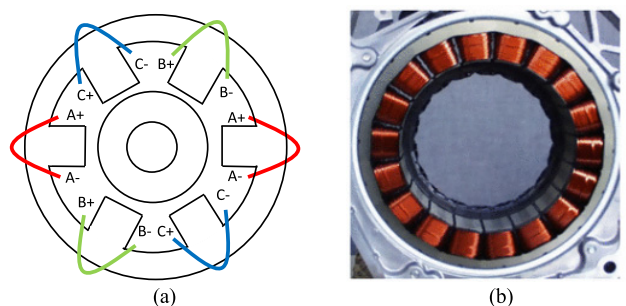
FIGURE 1. Sample FSCW-PMSM [2]. (a) Sample sketch of a 6 slots, 4 pole machine (b) Sample stator with concentrated coils.

Several approaches exist when designing FSCW-PMSMs. One approach relies on the designer experience and targets maximizing one performance metric such as the main harmonic winding factor [3] and follows a list of design rules which facilitate the machine design process [4]. Another approach relies on optimization design techniques, in which

typically an evolutionary optimization algorithm, such as Genetic Algorithm (GA) or Particle Swarm (PS) is coupled to a machine model which captures the machine's electromagnetic behavior, but can often include mechanical and thermal models as well [5]–[7].

Electric machine optimization design techniques have been applied in [7]–[12]. For instance in [8], a multi-objective optimization design of a surface mounted PMSM actuator for aero-space application was considered. Differential evolution algorithm was coupled with 2-D FEM and an analytical model for the leakage flux to enhance the performance in three machine performance metrics via variation of 5 degrees of freedom which are related to the machine geometry. However, the slot and pole number, air-gap, stack-length, stator and rotor radii's where fixed. For 48 generations, the simulation time was reported at almost 7 days. A somewhat similar approach was implemented in [9] with optimization algorithm coupled to 2-D FEA to design a PMSM for articulated robotics application.

An 18-slot, 16-pole machine was selected and then optimized based on considerations such as winding factor and switching frequency. In [10], a procedure to optimally design a surface-mounted (SM) FSCW-PMSM for an EV application was presented. The process takes into consideration the performance of the motor over a drive cycle and not just the rated operating point. The procedure was demonstrated on two machines with 12 slots but one with 10 poles rotor and the other with 14 poles rotor. A prototype was fabricated and was used to validate the predicted efficiency at different operating points, with very good match demonstrated.

In this work, a constrained multi-objective optimization design formulation for surface-mounted (SM) FSCW-PMSM is presented. The method is based on the work done in [11], where therein a rigorous multi-objective optimization problem was presented for an integer-slot distributed-winding (ISDW) SM-PMSM. The presented work, compared to aforementioned papers, has the advantage of being computationally efficient, based on analytical modelling, and thus with comparable accuracy to FEA methods [11], [12]. In addition, it allows incorporating a huge design space (22 parameters or more), which increases the probability of reaching a more optimum solution, and easily allows studying the effect of simultaneously changing the values of these parameters on the overall performance of the machine.

The paper is organized as follows. Section II, presents the machine analysis. Section III presents the formulation of the optimization problem, including the optimization space, constraints, and objectives. In Section IV, a case-study to design a motor with wide constant power speed range capability is presented, and the results are discussed. Validation of the results obtained from the analytical model is done in Section V via 2-D and 3-D FEA. Finally, Section VI includes the conclusion and recommended future work.
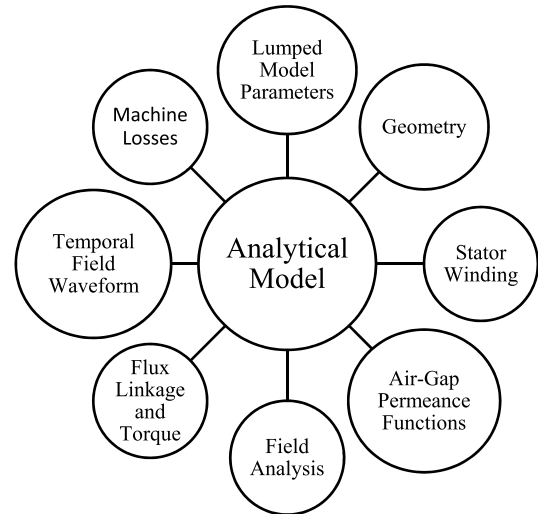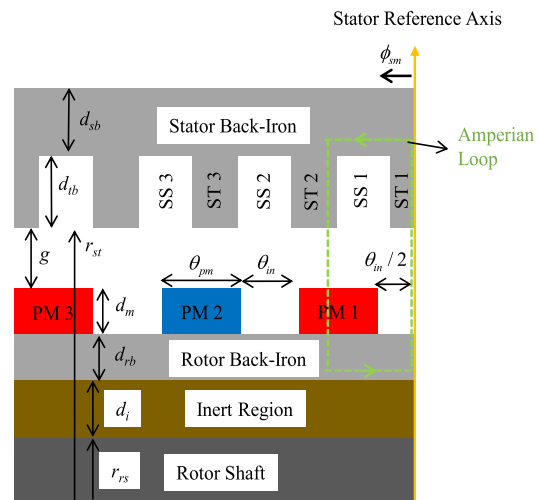
FIGURE 2. FSCW-PMSM analysis.

FIGURE 3. Developed diagram of part of the FSCW-PMSM at $\theta_{rm} = 0$.

II. MACHINE DESIGN

In this section, an analytical model that captures the electromagnetic behavior of a surface-mounted (SM) FSCW-PMSM is presented. Fig. 2 illustrates a block diagram of the main sections considered.

A. MACHINE DESIGN ANALYSIS

A generic developed diagram of a part of a surface mounted FSCW-PMSM is shown in Fig. 3. Positive rotor rotation is defined in the counter-clockwise direction, which translates to a linear movement towards the left. The spatial mechanical position around the machine ϕ_{sm} is defined with respect to the stator reference axis, which is defined to be located at the center of the first stator tooth (ST1). The rotor mechanical position θ_{rm} is defined with respect to the displacement of the rotor from the stator reference axis, with the rotor position shown in Fig. 3 set chosen as $\theta_{rm} = 0$.

The number of stator teeth and rotor poles are denoted by S_s and P, respectively. Red-colored permanent magnets (PMs) correspond to magnets magnetized in the negative radial direction (from stator to rotor), while blue magnets are magnetized in the positive radial direction. Conductors in the stator slots (SS) are not shown for clarity.

Also shown in Fig. 3 are the rotor shaft region with radius r_{rs}, inert material region with depth d_i, rotor back-iron region with depth d_{rb}, permanent magnets each with the depth of d_m, air gap between magnets and stator teeth g, depth of tooth base d_{tb}, and the stator back-iron with depth of d_{sb}. The radius to a stator tooth is equal to

$$r_{st} = r_{rs} + d_i + d_{rb} + d_m + g \tag{1}$$

The mechanical span of a permanent magnet and the region between two magnets are denoted by θ_{pm} and θ_{in}, respectively, and are given by

$$\theta_{pm} = \alpha_{pm} \frac{2\pi}{P} \tag{2}$$

$$\theta_{in} = \left(1 - \alpha_{pm}\right) \frac{2\pi}{P} \tag{3}$$

where α_{pm} is a fraction, theoretically between 0 and 1. Note that θ_{pm} plus θ_{in} gives the span of a rotor pole which is equal to $2\pi/P$. Expressions for the areas and volumes of different components of the machine in terms of the variables listed in Fig. 3 have been derived in [11]. Using these expressions, the total electromagnetic mass of the machine, that is the mass of active components, is calculated as

$$m_{tot} = V_{pm} \rho_{pm} + V_{st} \rho_{st} + V_{rb} \rho_{rb} + 3 V_w \rho_w \tag{4}$$

where V_{pm}, V_{st}, V_{rb} and V_w are the volumes of the permanent magnets, the stator iron (teeth and back-iron), rotor back-iron and the conductors of a single phase winding, respectively. The mass density of each component is denoted by ρ. Note that the last term in (4) is multiplied by three since a symmetrical three-phase machine is assumed. The remainder of the geometrical analysis is identical to what is presented in [11]. The next section considers the winding distribution of the stator and defines what is commonly known as the winding function.

B. STATOR WINDING

Herein, a concentrated three phase winding topology for a fractional slot machine is adopted. Note that the coil pitch of a concentrated winding is assumed to be equal to the stator slot pitch, that is $2\pi/S_s$.

Two common methods to devise the winding layout for FSCW machines are the star of slot method [13] and the method based on the decomposition of the number of slots per pole per phase [14]. The method described in [14] was chosen herein due to its relative simplicity and effectiveness.

The continuous winding function, which gives the number of turns around each stator tooth, can be generally expressed
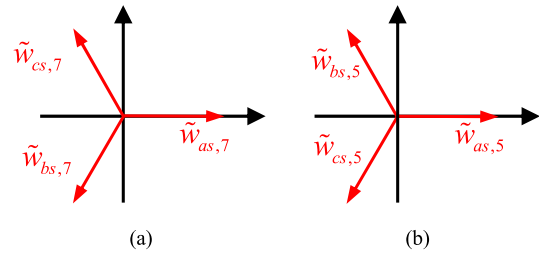
FIGURE 4. Phasor diagram of the continuous winding function fundamental component. (a) $S_S = 18$, $P = 14$ ($k_{fund} = 7$), (b) $S_S = 24$, $P = 20$ ($k_{fund} = 5$).

as an even function given by

$$\begin{bmatrix} \mathrm{w}_{as}(\phi_{sm}) \\ \mathrm{w}_{bs}(\phi_{sm}) \\ \mathrm{w}_{cs}(\phi_{sm}) \end{bmatrix} = N_{pc}\, w_k \begin{bmatrix} \cos\left(k\dfrac{n_{gcd}}{2}\phi_{sm}\right) \\ \cos\left(k\left(\dfrac{n_{gcd}}{2}\phi_{sm} - \gamma\dfrac{2\pi}{3}\right)\right) \\ \cos\left(k\left(\dfrac{n_{gcd}}{2}\phi_{sm} + \gamma\dfrac{2\pi}{3}\right)\right) \end{bmatrix} \tag{5}$$

where $\mathrm{w}_{as}(\phi_{sm})$, $\mathrm{w}_{bs}(\phi_{sm})$, $\mathrm{w}_{cs}(\phi_{sm})$ are the three-phase stator continuous winding functions. Note that with respect to notation throughout this paper, a variable y that depends on another variable x, will be written with non-italic font (i.e.: $\mathrm{y}(x)$).

Also in (5), N_{pc} is the number of conductors per coil, w_k is the Fourier series coefficient (summation '$\sum$' omitted for clarity), k is the harmonic number, and n_{gcd} is the greatest common divisor between the number of stator slots and rotor poles given by

$$n_{\mathrm{gcd}} = \gcd\left(S_s, P\right) \tag{6}$$

where $\gcd(x, y)$ is a function that returns the greatest common divisor between x and y. Finally, γ is an integer equal to 1 or -1 depending on whether the fundamental harmonic in the continuous winding function produces an 'abc' sequence excitation or an 'acb'. To further illustrate this, consider Fig. 4 which shows a phasor diagram of the fundamental component of the winding function for a sample 18-slot, 14-pole machine (a), and a sample 24-slot, 20 pole machine (b). Realizing that the fundamental harmonic component is equal to P/n_{gcd}, it can be seen that the former fundamental component follows an 'abc' sequence unlike the latter which forms an 'acb' sequence. Hence, a general procedure that ensures having 'abc' sequence regardless of the slot and pole combination is made possible using γ, which swaps the phasor location of the b-phase and c-phase phasors according to the following comparison

$$\mathrm{mod}\left(\frac{1}{3}\left(\frac{P}{n_{\mathrm{gcd}}} - 1\right), 1\right) \begin{cases} \neq 0 \Rightarrow \gamma = -1 \\ = 0 \Rightarrow \gamma = 1 \end{cases} \tag{7}$$

where $\mathrm{mod}(x, y)$ is a function that calculates the modulus after the division between x and y. A discrete winding vector, W_x, giving the number of turns per coil wound per stator

tooth can be derived from (5), where x stands for a-, b- or c-phase. Similarly, a discrete conductor distribution vector, N_x, giving the number of conductors per stator slot can be also derived from (5). Note that $w_x(\phi_{sm})$, W_x, and N_x are signed quantities, where the polarity indicates the direction of flux produced due to a positive current excitation in the conductors [11].

Finally, the packing factor in a stator slot for a double-layer concentrated winding can be expressed as

$$k_{pf} = \frac{2a_c N_{pc}}{a_{slt}} \tag{8}$$

where k_{pf} denotes the packing factor, a_c is the cross-sectional area of a conductor and a_{slt} is the surface area of a slot.

C. AIR-GAP PERMEANCE FUNCTION
A number of geometric and magnetic parameters, that influence the air-gap permeance, and eventually the air-gap flux density, are spatially periodic with respect to the angular position ϕ_{sm} and hence can be represented using Fourier series. These functions are the variation of the air-gap around the machine $g_v(\phi_{sm}, \theta_{rm})$, the variation of magnet thickness around the machine $d_{mv}(\phi_{sm}, \theta_{rm})$, the variation of the magnet remanence flux density around the machine $B_{mv}(\phi_{sm}, \theta_{rm})$, and the variation of the magnet relative permeability around the machine $\mu_{mv}(\phi_{sm}, \theta_{rm})$. Analytical expressions for these four functions can be found in [15].

D. FIELD ANALYSIS
The tempo-spatial air-gap flux density is calculated in this section with the following assumptions made. First, the MMF drop across the stator and rotor iron is neglected. This assumption is ensured by imposing saturation constraints on the stator and rotor iron as will be described in the next section. Second, in terms of cylindrical coordinates, the air-gap flux density vector is assumed to include only radial component, with the angular and axial components ignored. Third, the air-gap flux density within a tooth pitch is assumed to converge/diverge completely into/from the corresponding tooth, as depicted in Fig. 5. Fourth, the flux density flowing in a stator tooth is assumed to be uniform. Fifth, perfect control of the three-phase inverter drive is assumed. Finally, temperature variation effects are not considered.

Applying Ampere's law to the dotted green line shown in Fig. 3, and further simplifying, the stator MMF can be expressed as [11]

$$F_s = \int_{r_{rb}}^{r_{rb}+d_{mv}} H \, dr \;+\; \int_{r_{rb}+d_{mv}}^{r_{rb}+d_{mv}+g_v} H \, dr \tag{9}$$

where F_s is the stator MMF produced by the three-phase windings, r_{rb} is the radius to the rotor back-iron, and H is the field intensity. Note the functional dependency $(r, \phi_{sm}, \theta_{rm})$ was omitted in (9) for clarity. Following the derivation shown in [15], it can be shown that the air-gap flux density at any
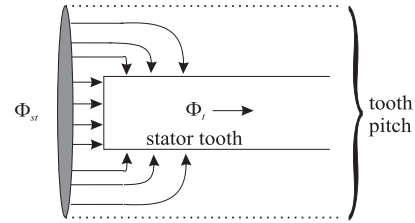

FIGURE 5. Stator tooth flux flow.

radial position between r_{rb} and r_{st} is given by

$$B_g(r, \phi_{sm}, \theta_{rm}) = \frac{r_{st}}{r}\left(\frac{F_s(\phi_{sm}, \theta_{rm}) + F_m(\phi_{sm}, \theta_{rm})}{R_g(\phi_{sm}, \theta_{rm}) + R_m(\phi_{sm}, \theta_{rm})}\right) \tag{10}$$

where F_m, R_g and R_m are the magnet MMF, air-gap quasi-reluctance and magnet quasi-reluctance, respectively. Expressions for these functions can be found in [15].

It is assumed that the inverter supplies a balanced, harmonic-free, three phase current of the form

$$\begin{bmatrix} i_{as}(\theta_{rm}) \\ i_{bs}(\theta_{rm}) \\ i_{cs}(\theta_{rm}) \end{bmatrix} = \sqrt{2}\,I_s \begin{bmatrix} \cos\left(\dfrac{P}{2}\theta_{rm} + \phi_i\right) \\ \cos\left(\dfrac{P}{2}\theta_{rm} + \phi_i - \dfrac{2\pi}{3}\right) \\ \cos\left(\dfrac{P}{2}\theta_{rm} + \phi_i + \dfrac{2\pi}{3}\right) \end{bmatrix} \tag{11}$$

where ϕ_i is the current vector position angle. Taking the dot product between (5) and (11) and simplifying, it can be shown that the three-phase stator MMF is equal to

$$F_s(\phi_{sm}, \theta_{rm}) = \frac{3\sqrt{2}}{2}I_s N_{pc}\left(f_s^1 + f_s^{u_+} + f_s^{u_-}\right) \tag{12}$$

where

$$f_s^1 = w_1 \cos\left(\frac{P}{2}\theta_{rm} + \phi_i + \gamma\frac{n_{gcd}}{2}\phi_{sm}\right) \tag{13}$$

$$f_s^{u_+} = w_{u_+} \cos\left(\frac{P}{2}\theta_{rm} + \phi_i + u_+\,\gamma\frac{n_{gcd}}{2}\phi_{sm}\right) \tag{14}$$

$$f_s^{u_-} = w_{u_-} \cos\left(\frac{P}{2}\theta_{rm} + \phi_i - u_-\,\gamma\frac{n_{gcd}}{2}\phi_{sm}\right) \tag{15}$$

and where $u_+ = 6j + 1$, $u_- = 6j - 1$ for $j = 1, 2, 3, 4 \ldots$.

E. FLUX LINKAGE, TORQUE, AND VOLTAGE
The q- and d-axes magnetizing flux linkages in the rotor frame of reference, not including the leakage component, can be calculated as

$$\begin{bmatrix} \lambda_{qm}^r \\ \lambda_{dm}^r \end{bmatrix} = 2r_{st}l \begin{bmatrix} \int_0^\pi B_g(r_{st}, \phi_{sm}, \theta_{rm})\, w_q(\theta_{rm}, \phi_{sm})\, d\phi_{sm} \\ \int_0^\pi B_g(r_{st}, \phi_{sm}, \theta_{rm})\, w_d(\theta_{rm}, \phi_{sm})\, d\phi_{sm} \end{bmatrix} \tag{16}$$

where the air-gap flux density in (10) is evaluated at $r = r_{st}$. Also therein, the qd continuous winding functions are obtained by multiplying (5) by the Park's reference frame

transformation matrix. Knowledge of (16) allows calculating the electromagnetic torque T_e and peak line-line voltage $v_{pk,l-l}$ which needs to be monitored so it doesn't exceed the dc-voltage source capabilities.

F. TEMPORAL FIELD WAVEFORMS

The temporal flux density in the stator steel is calculated assuming that all flux within a stator tooth converges/diverges completely into/out-off the stator tooth as shown in Fig. 5. Therein, Φ_{st} denotes the flux at $r = r_{st}$ and Φ_t denotes the flux flowing in the stator teeth. For stator tooth 1, equating $\Phi_{st} = \Phi_t$, and assuming a uniform flux density in the stator teeth, the temporal flux density is given by

$$B_{t,1}(\theta_{rm}) = \frac{r_{st} \, l \int_{\phi_{st1,st}}^{\phi_{st1,end}} B_g(r_{st}, \phi_{sm}, \theta_{rm}) \, d\phi_{sm}}{w_{tb} \, l} \quad (17)$$

where w_{tb} is the width of the tooth base and l is the stack length. Angles $\phi_{st1,st}$ and $\phi_{st1,end}$ are the starting and ending angular position of stator tooth 1. The temporal flux density in the stator tooth can be utilized to solve for the flux density in the stator and rotor back-irons, and the field intensity level in the permanent magnets as instructed in [11].

G. MACHINE LOSSES

Table 1 summarizes loss components considered in the design. These include the winding and semiconductors dc conduction losses, winding proximity and skin effect losses, core losses, and eddy-current loss in the permanent magnets. For the sake of maintaining the page count, more details and discussion about these models and variables involved can be found in the references listed next to each loss component.

The total loss P_l is found by adding the different loss components together

$$P_l = P_r + P_s + P_{ac,s} + P_{ac,p} + P_{pm} + p_{c,st}V_{stt} + p_{c,sb}V_{stb} \quad (18)$$

where V_{stt} and V_{stb} are the volumes of the stator teeth and stator back-iron, respectively.

H. LUMPED MODEL PARAMETERS

The q- and d-axis inductances, L_q and L_d, and the magnet flux linkage λ_m are obtained from (16) as follows with the listed excitation levels

$$L_d = L_{ls} + \frac{\lambda_{dm}^r}{i_{ds}^r}, \quad \left(i_{qs}^r = 0, \ i_{ds}^r = 1, \text{'Magnet off'}\right) \quad (19)$$

$$L_d = L_{ls} + \frac{\lambda_{dm}^r}{i_{ds}^r}, \quad \left(i_{qs}^r = 0, \ i_{ds}^r = 1, \text{'Magnet off'}\right) \quad (20)$$

$$\lambda_m = \lambda_{dm}^r, \quad \left(i_{qs}^r = 0, \ i_{ds}^r = 0, \text{'Magnet on'}\right) \quad (21)$$

where L_{ls} denotes the stator slot leakage inductance. The terms 'Magnet on' and 'Magnet off' refer to setting the amplitude of $B_{mv}(\phi_{sm}, \theta_{rm})$ to B_r or zero, respectively. The winding dc resistance is calculated using

$$R_{dc} = \frac{V_{xcs} + 2V_{xce}}{a_c \sigma_c} \quad (22)$$

TABLE 1. Machines losses.

Description	Equation
dc conduction loss (W) [11]	$P_r = 3I_s^2 R_{dc}$
Semi-conductor dc conduction loss (W) [11]	$P_s = \left(6\sqrt{2}\, v_{fs}I_s\right)/\pi$
Skin effect loss (W) [11]	$P_{ac,s} = 3I_s^2 R_{sk}$
Proximity effect loss (W) [11]	$P_{ac,p} = 3I_s^2 \left(\pi \sigma_c S_s l N_{pc}^3 \left(\frac{r_c^2 \mu_0 \omega_e}{6 w_{si}}\right)^2\right)$
Core loss density (W/m³) [20]	$p_{c,x} = f\left(k_h B_{x,\max}^\beta f_{eq}^{\alpha-1} + k_e \int_0^\tau \left(\frac{dB_x}{dt}\right)^2 dt\right)$
Magnet eddy current loss (W) [21]	$P_{pm} = \frac{K_{3D}P}{2}\left(\frac{r_{rg}^2 - r_{rb}^2}{2}\right)\frac{\theta_{PM}\, l}{\sigma_m \tau} \int_0^{\tau/P} J_m^2 dt$

where, V_{xcs} and V_{xce} are the volume of conductors occupying the stator slots and end-region, respectively. Expressions for L_{ls}, V_{xcs} and V_{xce} can be found in [11].

III. MULTI-OBJECTIVE OPTIMIZATION DESIGN

A multi-objective constrained optimization is formulated to design a FSCW-PMSM under a set of specifications and constraints. The optimization was carried through using a MATLAB based Genetic Algorithm (GA) toolbox, available in [17]. The following sub-sections describe the multi-objective optimization degrees of freedom, constraints, and objectives.

A. DEGREES OF FREEDOM

A total of 21 optimization degrees of freedom, also known as genes in GA terminology, are summarized in vector $\boldsymbol{\theta}$ shown below

$$\boldsymbol{\theta} = [s_t \ r_t \ c_t \ m_t \ n_{sp} \ d_i \ d_{rb} \ d_m \ g \ d_{tb} \ \alpha_t \ d_{sb} \ \alpha_{pm} \ l$$
$$N_{pc} \ u_{q,1} \ u_{d,1} \ u_{q,2} \ u_{d,2} \ \cdots \ u_{q,N_{op}} \ u_{d,N_{op}}] \quad (23)$$

Parameters s_t, r_t, c_t and m_t are integers used to establish a mapping between the stator, rotor, conductor and magnet materials, respectively, and a database that contains the properties of different steel, conductor and permanent magnet materials [11], [12]. Parameter n_{sp} is an integer which maps into a pair of prechosen S_s and P combinations. The span of the stator tooth compared to the total tooth pitch is set by fraction α_t. Parameter N_{pc} is the number of conductors per coil. The required q- and d-axis currents necessary to obtain the target torque while satisfying the imposed constraints are found using the following control laws [18]

$$i_{qs,o}^r = u_{q,o}\frac{4T_{e,o}^*}{3P\lambda_m} \quad (24)$$

$$i_{ds,o}^r = u_{d,o}\frac{\lambda_m}{L_d} \quad (25)$$

where subscript o denotes the operating point number, $T_{e,o}^*$ denotes the target torque at operating point o, and $u_{q,o}$ and

TABLE 2. Design constraints.

Constraint	Description
$c_1 = \text{ltn}\left(d_{tb}/w_{tb}, \alpha_{tar}\right)$	Tooth aspect ratio less than α_{tar}
$c_2 = \text{ltn}\left(d_m/\left(r_{rb}\theta_{pm}\right), \alpha_{mar}\right)$	Magnet aspect ratio less than α_{mar}
$c_3 = \text{ltn}\left(d_c\alpha_{so}, w_{so}\right)$	Slot opening constraint
$c_4 = \text{ltn}\left(m_{tot}, m_{\lim}\right)$	Max mass limit
$c_5 = \text{ltn}\left(r_{rb}\max(\omega_{rm}), v_{tp,mx}\right)$	Max rotor tip speed
$c_6 = \text{ltn}\left(\max\left(J_s\right), J_{\lim}\right)$	Max current density limit
$c_7 = \text{ltn}\left(\max(\sqrt{2}I_s), I_{mx}\right)$	Max peak current limit [23]
$c_8 = \text{ltn}\left(v_{pk,l-l,o}, v_{dc} - 2v_{fs}\right)$	Max peak line-line voltage limit
$c_9 = \text{ltn}\left(P_{l,o}, P_{l,\lim}\right)$	Max total loss per op. point limit
$c_{10} = \text{gtn}\left(T_{ec,o}, T_{e,o}^*\right)$	Max corrected torque limit
$c_{11} = \text{ltn}\left(B_{t1,mx,o}, B_{\lim}\right)$	Max peak tooth flux density limit
$c_{12} = \text{ltn}\left(B_{sb1,mx,o}, B_{\lim}\right)$	Max peak stator back-iron limit
$c_{13} = \text{ltn}\left(B_{rbr1,mx,o}, B_{\lim}\right)$	Max peak radial rotor back-iron limit
$c_{14} = \text{ltn}\left(B_{rbt1,mx,o}, B_{\lim}\right)$	Max peak tangential rotor back-iron limit
$c_{15} = \text{ltn}\left(H_{pm,mn,o}, k_m H_{ci}\right)$	Min magnet field intensity limit

FIGURE 6. FSCW-PMSM design operating points.

TABLE 3. General design specifications.

Property	Value	Property	Value
v_{dc}	400 V	$v_{tp,mx}$	200 m/s
k_{pf}	0.5	k_m	0.75
v_{fs}	2 V	$m_{\lim}$	14 kg
r_{rs}	2 cm	$P_{l,\lim}$	500 W
α_{tar}	10	$J_{\lim,Cu}$	7.6 A/mm^2
α_{mar}	0.4	$B_{\lim,M19}$	1.39 T
α_{so}	1.5		

$u_{d,o}$ are control fractions for each operating point. Note that this formulation is generalized for N_{op} operating points, and hence N_{op} pairs of current control fractions are included. The remaining parameters in (23) are mainly geometric and have been defined in Fig. 3.
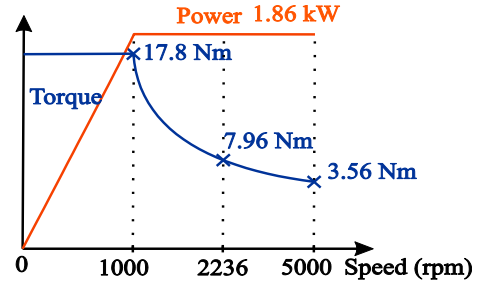
B. DESIGN CONSTRAINTS

A number of constraints are added to ensure obtaining a proper design. These constraints are imposed using a 'less-than' ltn $(x, x_{\max})$ and 'greater-than' gtn $(x, x_{\min})$ functions, defined in [11]. Each function works by comparing the input value x to the threshold value. If the constraint is satisfied ($x < x_{\max}$ or $x > x_{\min}$), both functions return a value equal to 1. However, if this was not the case, both functions return a value less than 1 that approaches zero the greater the difference is between x and the upper or lower limits. Applied constraints are listed in Table 2 along with a brief description. Further information on all constraints can be found in [11], [12] and [18].

C. OPTIMIZATION OBJECTIVES

Two objectives considered for this optimization are minimizing the electromagnetic mass, (4), and minimizing the weighted power loss. The weighted loss is given by the following dot product

$$P_{lw} = \left[P_{l,1}, P_{l,2}, \dots P_{l,N_{op}}\right]\left[w_1, w_2, \dots w_{N_{op}}\right]^T \quad (26)$$

where superscript T denotes vector transpose operation. The first vector is the power loss for each operating point treated in the optimization and calculated from (18). The second vector

is a weighting vector that sums to 1 and is used to weigh each operating point.

The fitness function, also known as cost function, is evaluated as follows. Defining C_S, C_I, and N_C as the number of constraints satisfied, the number of constraints evaluated, and the total number of constraints, the fitness function is defined as

$$f(\boldsymbol{\theta}) = \begin{cases} \varepsilon\left(\dfrac{C_S - N_C}{N_C}\right)\begin{bmatrix} 1 \\ 1 \end{bmatrix} & C_S < C_I \\[4mm] \left[\dfrac{1}{m_{tot}} \quad \dfrac{1}{P_{lw}}\right]^T & C_S = N_C \end{cases} \quad (27)$$

where ε is a very small number (e.g.: 10^{-10}). Until all constraints are satisfied ($C_S = N_C$) a small negative number is assigned to the fitness vector. Otherwise, the fitness function vector is calculated as the reciprocal of mass and weighted loss, since the optimization engine is coded to maximize the objectives. An extended discussion on the construction of fitness functions can be found in [11].

IV. DESIGN CASE STUDY

A 1.86 kW FSCW-PMSM motor driven from a three-phase inverter is designed using the procedure set forth in the previous sections. The demanded torque at three operating speeds is shown in Fig. 6. The motor should deliver a constant 1.86 kW power over a wide speed range ratio of 5:1. General design specifications and constraints limits are listed in Table 3. The current density and flux density limits are based on the recommended values for Copper and M19 steel type [13].

TABLE 4. GA gene range.

Gene	Min.	Max.	Inc. Type	Gene	Min.	Max.	Inc. Type
s_t	1	1	Int.	d_{sb}	1 mm	8 cm	Log.
r_t	1	1	Int.	α_{pm}	0.3	0.8	Lin.
c_t	1	1	Int.	l	1 cm	50 cm	Log.
m_t	1	7	Int.	N_{pc}	5	25	Lin.
n_{sp}	1	3	Int.	$\alpha_{q,1}$	0.1	1.5	Lin.
d_i	1 mm	10 cm	Log.	$\alpha_{d,1}$	-0.2	0	Lin.
d_{rb}	1 mm	8 cm	Log.	$\alpha_{q,2}$	0.1	1.5	Lin.
d_m	1 mm	5 cm	Log	$\alpha_{d,2}$	-1	0	Lin.
g	0.5mm	4 mm	Log.	$\alpha_{q,3}$	0.1	1.5	Lin.
d_{tb}	1 mm	8 cm	Log.	$\alpha_{d,3}$	-1	0	Lin.
α_t	0.2	0.95	Lin.				

TABLE 5. Winding function fourier series coefficients.

Slots and Poles	w_k
$S_s = 12, P = 10$	$\dfrac{4}{k\pi}\sin\left(\dfrac{k\pi}{2}\right)\left(1 - \cos\left(k\theta_{stp}\right)\right)$
$S_s = 18, P = 14$	$\dfrac{4}{k\pi}\sin\left(\dfrac{k\pi}{2}\right)\left(\cos\left(k\left(\pi - \theta_{stp}\right)/2\right) - 2\sin\left(k\theta_{stp}/2\right)^2\right)$
$S_s = 24, P = 20$	$\dfrac{4}{k\pi}\sin\left(\dfrac{k\pi}{2}\right)\left(1 - \cos\left(k\theta_{stp}\right)\right)$

Note that the three operating points are weighed equally for this design study.

Table 4 gives the maximum and minimum limits on each optimization gene vector (23). Also shown therein, is the type of incrimination between the minimum and maximum values which can be 'Integer', 'Linear' or 'Logarithmic' [13]. Note that in order to limit the design space, parameters 1-3 were intentionally fixed to 1 by setting the minimum and maximum values to 1, which maps to 'M19' steel type for the stator and rotor steels, and Copper for the winding conductor material. The magnet type gene m_t can be mapped to 7 magnet types such as AlNiCo, SmCo, NdFeB and Ferrite magnets. Information on relevant properties of each permanent magnet type such as the remanent flux density and intrinsic coercivity can be found in [12]. The stator slots and poles combination gene n_{sp} can map to three different combinations which are $(S_s, P) = (12,10)$ and $(18,14)$ or $(24,20)$. Expressions for the winding function Fourier series coefficient w_k for these combinations are given in Table 5. Therein, angle θ_{stp} is given by

$$\theta_{stp} = n_{\text{gcd}} \frac{2\pi}{S_s} \tag{28}$$

Note that all coefficients in Table 5 are non-zero for odd harmonics only. The range on the remaining genes were selected based on previous work [12].
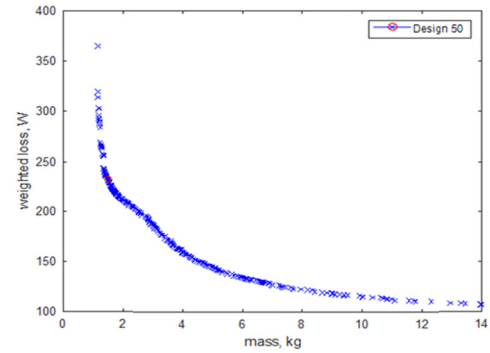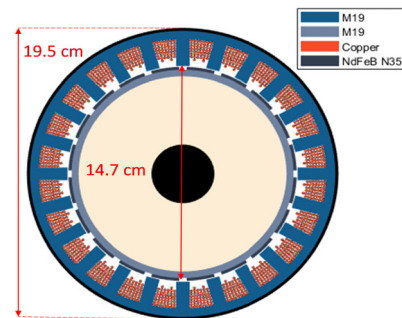

FIGURE 7. Pareto optimal front.

FIGURE 8. Cross-section of design number 50.

The multi-objective optimization was run on a desktop PC with 28 local core workers. The number of generations and populations were set to 3000 each. Results were obtained after 7 hours, with around 7.5 million fitness function evaluations.

The Pareto-optimal front of weighted loss versus mass is shown in Fig. 7. Therein, each point represents a complete FSCW-PMSM design satisfying all imposed design specs and constraints. Machines with heavier mass produce less weighted loss and vice versa. After closer inspection, it was found that all machines in the front are 24-slot, 20-pole machines. Compared to the two other slot and pole combinations, increasing the number of poles allows reducing the thickness of the stator and rotor back-irons which leads to a reduction of the overall machine's mass. However, a higher pole count results in an increase in semiconductor switching losses and core losses, where the former was not considered in this work.

Machine design 50, labeled with a red circle in Fig. 7, with a mass of 11.8 kg and weighted loss of around 240 W was selected for a closer inspection. The cross-section is shown in Fig. 8. The legend displays the material type for the steel, conductors, and magnet. A number of characteristics for this machine are listed in Table 6.

V. FEA VALIDATION

A 2-D and 3-D ANSYS Maxwell FEA [23] models of design number 50 was built and analyzed for comparison. Fig. 9

TABLE 6. Machine 50 characteristics.

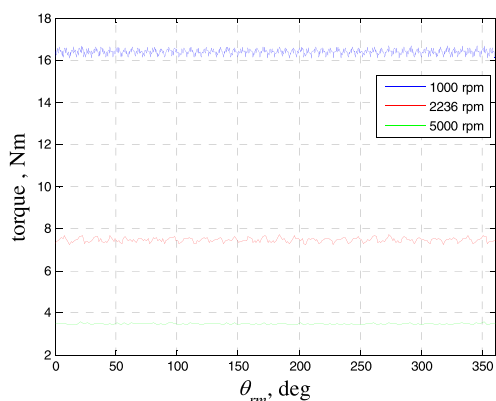| Parameter	Value	Parameter	Value
d_i	46.3 mm	R_{dc}	151 mΩ
d_{rb}	4.5 mm	L_q	0.96 mH
d_m	2.02 mm	L_d	0.96 mH
g	0.5 mm	λ_m	43.8 mVs
d_{tb}	18.3 mm	i_{qs}^r	[26.9 12.2 5.92] A
d_{sb}	5.79 mm	i_{ds}^r	[-5.41 -4.61 -6.14] A
l	1.76 cm	I_s	[19.4 8.6 4.2] A
N_{pc}	25	J_s	[7.37 3.51 2.3] A/mm^2
d_c	1.83 mm	$v_{pk,l-l}$	[94.0 174 357] V
α_{pm}	0.79	P_l	[313 163 271] W

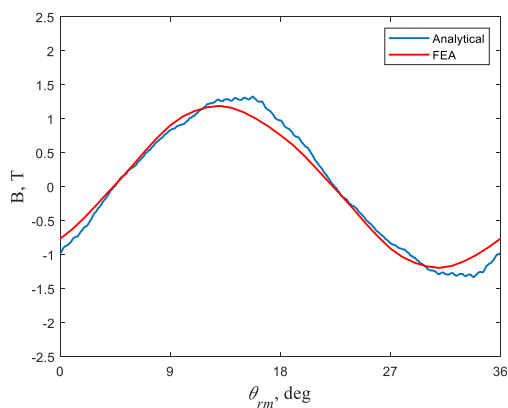**FIGURE 9.** Transient FEA torque waveforms for operating points 1-3.

FIGURE 10. Stator tooth 1 flux density versus rotor position from analytical and FEA model at 1000 rpm.

displays the torque waveforms for all three operating points, obtained from a transient simulation. The average torque for each trace is close to the required value with a maximum peak to peak ripple of 0.47 Nm at 1000 rpm. Fig. 10 compares the analytically calculated average flux density waveform in stator teeth 1 (17) to that measured in the FEA model. Very close agreement between the waveforms is obtained. This indirectly validates the saturation and core loss calculations;

TABLE 7. Analytical and FEA model predictions AT $\theta_{rm} = 0$.

Parameter	Analytical	FEA
L_q	0.96 mH	1.07 mH
L_d	0.96 mH	1.08 mH
λ_m	43.76 mVs	41.33 mVs

however, more tests and measurements are needed to reach a definitive conclusion. Lumped model parameters from 3-D FEA are compared to those obtained analytically in Table 7. Good agreement in results is achieved.

VI. CONCLUSION AND FUTURE WORK

This work presented a generic analytical multi-objective constrained optimization design procedure for a surface-mounted fractional-slot concentrated-winding permanent magnet synchronous machine (SM FSCW-PMSM). A comprehensive analytical model which takes into account various aspects of the machine such as machine geometry, spatial and temporal fields and various loss components was presented and thoroughly discussed. Next, the formulation of a multi-objective constrained optimization problem to design an optimum FSCW-PMSM for wide constant power speed application was presented. The optimization results demonstrated the accuracy of the proposed model with comparison to numerical models such as FEA, but with much faster computational performance which makes it much more suitable to be used in evolutionary optimization design approaches.

Future work should generalize the proposed model to include single-layer winding topologies and more slot and pole combinations. Additionally, magnet-magnet leakage flux should be studied and included. Modelling of semiconductor switching losses will be included in the future to have a much better comparison between machine drive structures with differing number of poles. Another effect which requires more attention is the performance of the proposed model under magnetic saturation. In this case the imposed constraints on saturation will be relaxed. Finally, experimental validation on a prototype FSCW-PMSM will be conducted.

REFERENCES

[1] C. M. Spargo, B. C. Mecrow, J. D. Widmer, and C. Morton, "Application of fractional-slot concentrated windings to synchronous reluctance motors," *IEEE Trans. Ind. Appl.*, vol. 51, no. 2, pp. 1446–1455, Apr. 2015.

[2] A. M. El-Refaie, "Fractional-slot concentrated-windings synchronous permanent magnet machines: Opportunities and challenges," *IEEE Trans. Ind. Electron.*, vol. 57, no. 1, pp. 107–121, Jan. 2010.

[3] N. Bekka, M. El Hadi Zaïm, N. Bernard, and D. Trichet, "A novel methodology for optimal design of fractional slot with concentrated windings," *IEEE Trans. Energy Convers.*, vol. 31, no. 3, pp. 1153–1160, Sep. 2016.

[4] R. Dutta, L. Chong, and M. F. Rahman, "Design and experimental verification of an 18-Slot/14-pole fractional-slot concentrated winding interior permanent magnet machine," *IEEE Trans. Energy Convers.*, vol. 28, no. 1, pp. 181–190, Mar. 2013.

[5] X. Zhang, W. Li, B. Kou, J. Cao, H. Cao, C. Gerada, and H. Zhang, "Electrothermal combined optimization on notch in air-cooled high-speed permanent-magnet generator," *IEEE Trans. Magn.*, vol. 51, no. 1, Jan. 2015, Art. no. 8200210.

[6] Z. Huang and J. Fang, "Multiphysics design and optimization of high-speed permanent-magnet electrical machines for air blower applications," *IEEE Trans. Ind. Electron.*, vol. 63, no. 5, pp. 2766–2774, May 2016.

[7] P. Akiki, M. H. Hassan, M. Bensetti, P. Dessante, J.-C. Vannier, D. Prieto, and M. McClelland, ''Multiphysics design of a V-shape IPM motor,'' *IEEE Trans. Energy Convers.*, vol. 33, no. 3, pp. 1141–1153, Sep. 2018.

[8] M. E. Beniakar, A. G. Sarigiannidis, P. E. Kakosimos, and A. G. Kladas, ''Multiobjective evolutionary optimization of a surface mounted PM actuator with fractional slot winding for aerospace applications,'' *IEEE Trans. Magn.*, vol. 50, no. 2, pp. 665–668, Feb. 2014.

[9] D.-K. Hong, W. Hwang, J.-Y. Lee, and B.-C. Woo, ''Design, analysis, and experimental validation of a permanent magnet synchronous motor for articulated robot applications,'' *IEEE Trans. Magn.*, vol. 54, no. 3, pp. 1–4, Mar. 2018.

[10] J. Wang, X. Yuan, and K. Atallah, ''Design optimization of a surface-mounted permanent-magnet motor with concentrated windings for electric vehicle applications,'' *IEEE Trans. Veh. Technol.*, vol. 62, no. 3, pp. 1053–1064, Mar. 2013.

[11] S. D. Sudhoff, *Power Magnetic Devices: A Multi-Objective Design Approach*. Hoboken, NJ, USA: Wiley, Feb. 2014.

[12] J. Y. Alsawalhi and S. D. Sudhoff, ''Design optimization of asymmetric salient permanent magnet synchronous machines,'' *IEEE Trans. Energy Convers.*, vol. 31, no. 4, pp. 1315–1324, Dec. 2016.

[13] N. Bianchi and M. D. Pre, ''Use of the star of slots in designing fractional-slot single-layer synchronous motors,'' *IEEE Proc.-Electr. Power Appl.*, vol. 153, no. 3, pp. 459–466, May 2006.

[14] J. Cros and P. Viarouge, ''Synthesis of high performance PM motors with concentrated windings,'' *IEEE Trans. Energy Convers.*, vol. 17, no. 2, pp. 248–253, Jun. 2002.

[15] S. O. Edhah and J. Y. Alsawalhi, ''Air gap flux density analytical model for a fractional-slot concentrated-winding SM-PMSM,'' in *Proc. IEEE Int. Conf. Elect. Syst. Aircr., Railway, Ship Propuls. Road Vehicles Int. Transp. Electrific. Conf. (ESARS-ITEC)*, Nottingham, U.K., Nov. 2018, pp. 1–6.

[16] O. Laldin, S. D. Sudhoff, and S. Pekarek, ''Modified Carter's coefficient,'' *IEEE Trans. Energy Convers.*, vol. 30, no. 3, pp. 1133–1134, Sep. 2015.

[17] (Nov. 2017). *Genetic Optimization System Engineering Tool (GOSET) for Use With MATLAB*. [Online]. Available: https://engineering.purdue.edu/ECE/Research/Areas/PEDS/go_system_engineering_toolbox

[18] J. A. Krizan and S. D. Sudhoff, ''A design model for salient permanent-magnet machines with investigation of saliency and wide-speed-range performance,'' *IEEE Trans. Energy Convers.*, vol. 28, no. 1, pp. 95–105, Mar. 2013.

[19] G. M. Shane and S. D. Sudhoff, ''Refinements in anhysteretic characterization and permeability modeling,'' *IEEE Trans. Magn.*, vol. 46, no. 11, pp. 3834–3843, Nov. 2010.

[20] J. Reinert, A. Brockmeyer, and R. W. A. A. De Doncker, ''Calculation of losses in ferro- and ferrimagnetic materials based on the modified Steinmetz equation,'' *IEEE Trans. Ind. Appl.*, vol. 37, no. 4, pp. 1055–1061, Jul. 2001.

[21] A. L. Rodríguez, D. J. Gómez, I. Villar, A. López-de-Heredia, and I. Etxeberria-Otadui, ''New analytical method for PMSM magnet losses estimation based on Fourier series,'' in *Proc. Int. Conf. Elect. Mach. (ICEM)*, Berlin, Germany, Sep. 2014, pp. 1314–1320.

[22] *Power Stream*. Accessed: Feb. 23, 2019. [Online]. Available: https://www.powerstream.com

[23] *ANSYS Maxwell*. Accessed: Mar. 19, 2019. [Online]. Available: http://www.ansys.com/

SALEH O. EDHAH (S'15) received the B.S. and M.S. degrees in electrical engineering from Khalifa University, in 2016 and 2018, respectively. He is currently pursuing the Ph.D. degree with the Khalifa University of Science and Technology, United Arab Emirates.

JAMAL Y. ALSAWALHI (S'12–M'14) received the B.S., M.S., and Ph.D. degrees in electrical engineering from Purdue University, in 2009, 2011, and 2014, respectively. He is currently an Assistant Professor of electrical engineering with Khalifa University, United Arab Emirates. His interest includes electrical machines design and analysis for transportation electrification application.

AHMED A. AL-DURRA received the Ph.D. degree in ECE from Ohio State University, in 2010. He is currently an Associate Professor with the ECE Department, Khalifa University, United Arab Emirates. He has one U.S. patent, one edited book, 12 book chapters, and over 170 scientific articles in top-tier journals and refereed international conference proceedings. He has supervised/co-supervised over 20 Ph.D./master's students. His research interests are applications of control and estimation theory on power systems stability, micro and smart grids, renewable energy systems and integration, and process control. He is also leading the Energy Systems, Control and Optimization Lab at ADNOC Research and Innovation Center, an Editor of the IEEE TRANSACTIONS ON SUSTAINABLE ENERGY and the IEEE POWER ENGINEERING LETTERS, and an Associate Editor for the IEEE TRANSACTIONS ON INDUSTRY APPLICATIONS and *Frontiers in Energy Research–Smart Grids*.

• • •